Chemical Science

ROYAL SOCIETY OF CHEMISTRY

EDGE ARTICLE

View Article Online
View Journal | View Issue

Check for updates

Cite this: *Chem. Sci.*, 2022, **13**, 6335

All publication charges for this article have been paid for by the Royal Society of Chemistry

Customising excitation properties of polycyclic aromatic hydrocarbons by rational positional heteroatom doping: the *peri*-xanthenoxanthene (PXX) case†

Cataldo Valentini,[a] Duncan Gowland,[b] C. Grazia Bezzu,[a]
Deborah Romito,[c] Nicola Demitri,[d] Nicola Bonini*[b] and Davide Bonifazi*[ac]

In this paper we tackle the challenge of gaining control of the photophysical properties of PAHs through a site-specific N-doping within the structural aromatic framework. By developing a simple predictive tool that identifies C(sp^2)-positions that if substituted with a heteroatom would tailor the changes in the absorption and emission spectral envelopes, we predict optimal substitutional patterns for the model *peri*-xanthenoxanthene (**PXX**) PAH. Specifically, TDDFT calculations of the electron density difference between the S_1 excited state and S_0 ground state of **PXX** allowed us to identify the subtleties in the role of sites *i.e.*, electron donating or withdrawing character on excitation. The replacement of two C(sp^2)-atoms with two N-atoms, in either electron donating or withdrawing positions, shifts the electronic transitions either to low or high energy, respectively. This consequently shifts the **PXX** absorption spectral envelop bathochromically or hypsochromically, as demonstrated by steady-state absorption spectroscopic measurements. Within the series of synthesised N-doped **PXX**, we tune the optical band gap within an interval of ~0.4 eV, in full agreement with the theoretical predictions. Relatedly, measurements show the more blueshifted the absorption/emission energies, the greater the fluorescence quantum yield value (from ~45% to ~75%). On the other hand, electrochemical investigations suggested that the N-pattern has a limited influence on the redox properties. Lastly, depending on the N-pattern, different supramolecular organisations could be obtained at the solid-state, with the 1,7-pattern **PXX** molecule forming multi-layered, graphene-like, supramolecular sheets through a combination of weak H-bonding and π–π stacking interactions. Supramolecular striped patterned sheets could also be formed with the 3,9- and 4,10-congeners when co-crystallized with a halogen-bond donor molecule.

Received 17th February 2022
Accepted 27th April 2022

DOI: 10.1039/d2sc01038k

rsc.li/chemical-science

Introduction

Polycyclic aromatic hydrocarbons (PAHs) are attracting great interest in the recent years for preparing organic semiconductors that, absorbing in the UV-vis spectral range of solar irradiation, generate excited states of interest for light-harvesting applications[1] and photocatalysis.[2–5] Capitalising on the wealth of organic synthetic methodologies, chemists have tailored the photophysical properties of PAHs by: (i) changing the size and edge of the aromatic scaffold; (ii) varying the molecular planarity; (iii) changing the resonance energy of the constituting monomeric units; (iv) varying the peripheral functionalisation of the edges through the insertion of either electron-donating or -withdrawing substituents; (v) replacing C(sp^2) atoms by isostructural analogues, *i.e.*, heteroatom doping.[6–9] Amid all approaches, the doping route can effectively tailor the photophysical properties of a PAH without the need to add peripheral groups while maintaining the structural topology.[7,9] It is thus expected that one can encode the functionalization that defines the photochemistry of PAHs *via* a site-specific substitutional pattern. Owing to the possibilities of introducing the heteroatom in different ratios ($\rho = \dfrac{n(d)}{n(d) + d(C)} \times 100$, where $n(d)$ and $d(C)$ are the numbers of

---

[a] *School of Chemistry, Cardiff University, Main Building, Park Place, Cardiff CF10 3AT, UK*

[b] *Department of Physics, King's College London, Strand, London, WC2R 2LS, UK. E-mail: nicola.bonini@kcl.ac.uk*

[c] *Institute of Organic Chemistry, Faculty of Chemistry, University of Vienna, Währinger Str. 38, 1090, Vienna, Austria. E-mail: davide.bonifazi@univie.ac.at*

[d] *Elettra – Sincrotrone Trieste, S.S. 14 Km 163.5 in Area Science Park, 34149 Basovizza, Trieste, Italy*

† Electronic supplementary information (ESI) available: Experimental procedures, additional transient absorption data, synthetic and computational details, and X-ray crystallographic data. CCDC 1985339 (**1,7-*N,N*-PXX**), 1985342 (**3,9-*N,N*-PXX**), 1985344 (**4,10-*N,N*-PXX**), 2133474 (**4,10-*N,N*-PXX·DITFB**), 2133475 (**3,9-*N,N*-PXX·DITFB**) and 2151478 (**3**). For ESI and crystallographic data in CIF or other electronic format see **https://doi.org/10.1039/d2sc01038k**

doping heteroatom and carbons), positions, and symmetries, numerous configurations are possible even for small PAHs. While the general influence on the energy level of the frontier molecular orbitals of replacing a C(sp^2) atom with a more electronegative heteroatom such as N is well established (*i.e.*, lower-energy rigid shift of the HOMO and LUMO levels),[10–21] it is more difficult to predict the influence of tailoring heteroatom position on optoelectronic properties.[22,23] Herein, we raise the question of whether it is possible to rationally customise optical bandgap properties of a PAH by a specific heteroatom doping pattern and if this can be conceived *a priori*. In the absence of any formalized approach to conceive a tailored doping pattern, we would need synthesise and analyse each positional congeners to establish a structure–property relation. Considering the large number of possible doping patterns, this trial-and-error approach could result in a substantial amount of unnecessary synthetic efforts. To minimise these efforts, one needs a predictive tool that identifies those C(sp^2)-positions in the PAH core that, if substituted with a heteroatom, would induce the desired changes in the absorption and emission spectral envelopes. It is with this challenge in mind that we have developed a simple conceptual approach that would allow organic chemists to devise pertinent heteroatom-doping patterns to rationally tune the absorption UV-vis envelope of a given PAH. Using *peri*-xanthenoxanthene (**PXX**) as a model PAH, herein we show that one can predictably tailor its UV-vis absorption and emission energies through specific substitutional patterns using N-atoms as dopants.

Results and discussions

The concept: use of charge-redistribution maps for rational heteroatom doping

We wish to develop a rational tool that allows organic chemists to tailor the optical gap of a given PAH through specific heteroatom doping patterns. Tailored absorption and emission properties could in principle be obtained by simply gaining control of the ground (PAH, S$_0$) and excited (PAH*, S$_1$, the first bright singlet excited state in this case) state energies and properties through chemical functionalisation (*e.g.*, controlling the HOMO and LUMO energies and their overlaps). In a simplified picture, one can envisage that introducing a dopant which destabilises the electronic excited state (PAH*, S$_1$) whilst keeping the ground state energy fixed leads to an opening of the optical gap, *i.e.*, a hypsochromic shift in the spectral envelop. Of course, this primitive model is highly limited as all properties (both electronic and geometric) of a molecule are intimately related to the exact atomic composition and positions – the ground state energies and structural properties are not the same for different positional isomers.

In the general case of a rigid molecule, it is reasonable to hypothesise a negligible structural distortion due to heteroatom doping and/or on excitation (this is discussed further in our results). This would allow one to more directly compare the electronic excitation properties of different doping patterns (*i.e.*, a direct calculation and comparison of the S$_0$ → S$_1$ transition). The latter statement, that geometries vary little on excitation, is related to the Franck–Condon approximation, which in this case is assumed as we require that not only the ground state structures of the positional isomers are similar, but that their excited state dynamics are also similar. Following these approximations, we note the influence of the heteroatom position can be subtle but significant on both the ground and excited states. For example, visualisation or quantification of different regioisomer HOMO and LUMO orbitals can reveal little trend in their structure and one would have to understand the trends in both to make predictions about the optical gap. Therefore, we move to directly examining the properties of excitations rather than states, which more clearly would allow identification in trends on optical properties. More specifically, we calculate and utilise a charge redistribution 'map' (related to the TDDFT density difference) on excitation of the PAH structure to identify electronic withdrawing and donating domains, allowing prediction of whether replacing specific C(sp^2) atoms would either favour or disfavour the charge redistribution and could induce an energy shift of the electronic transition. This methodology is powerful as it allows rich comparison and can incorporate changes to both ground and excited state electronic and structural properties between isomers. Thus, the idea is to map the charge redistribution between the S$_0$ and S$_1$ states and use it as the matrix to rationalise the choice of a given doping pattern.

Our case study: rational N-doping of PXX

Our group is involved in synthetic programs developing O-doped PAH chromophores.[24–27] One of our targets is **PXX** (Fig. 1), the O-containing analogue of anthanthrene.[3,28–33] Considering the vis-absorbing bandgap, with minor Stokes shift and good emission properties ($\Phi_F = 60\%$) of **PXX** (Fig. 1), we envisioned that the replacement of one or more C(sp^2)-atoms with N-atoms could affect its optical bandgap.

This conjecture led us to design a series of N-doped **PXX** derivatives (***N*,*N*-PXX**, featuring a ρ value of 9%), in which two N-

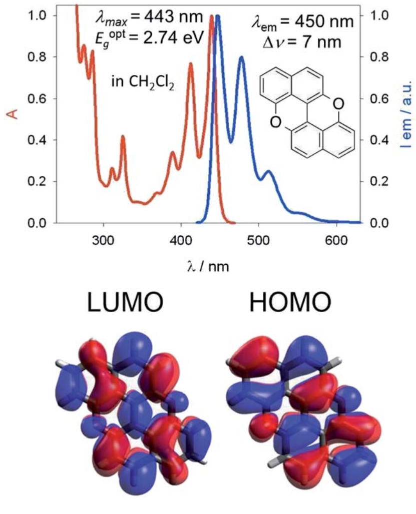

Fig. 1 Structural framework of PXX along with its fundamental optical gap properties.

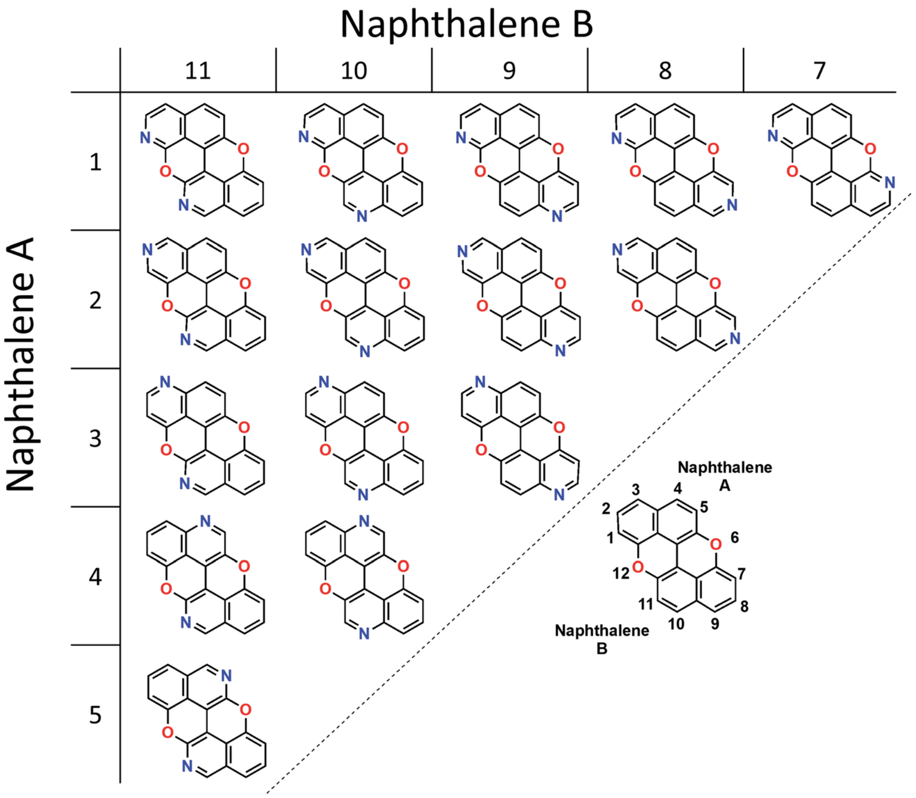

Fig. 2 Positional isomers of *N*,*N*-PXX, where the N-atoms are peripherally localised.

atoms replace specific C(sp^2)–H functions at the peripheries (Fig. 2). Given the large number of positional possibilities, here we focused our attention on ***N*,*N*-PXX** regioisomers bearing one N-atom for each naphthalenyl ring (Fig. 2). This provides a way to explore a reasonable variety of structures at fixed doping ratio (ρ). For the **PXX** molecule and the set of regioisomers, we performed *ab initio* calculations at the TD-/DFT/B3LYP/6-311+G* level of theory in Gaussian 09 (the accuracy of these and further computational details are discussed below and in the ESI†).[34–40] For these systems we find that the first excited state (S_1) is bright and energetically well separated from the second state (S_2) that is consistently much darker. Our calculations also suggest that **PXX** and its N-doped congeners do not experience any significant conformational change in either the ground state or on electronic transition.

Therefore, we moved to directly comparing excitations. The unique methodology we employ to compare excitations is based on calculating the set of atomic point charges (in the CHELPG formalism[41]) of the ground and excited state and examining the difference (Fig. 3). This difference is then interpolated across the space of the molecule to create the 2D maps which show how many electrons are gained or lost around an atom on excitation. The accuracy of these maps is examined in the ESI,† where we compare it to more physical quantities, such as the exact TDDFT density differences and molecular orbitals. As shown in the charge redistribution map of **PXX** (Fig. 3), the peripheral C-atoms display a significant and unequal electron redistribution upon the electronic transition. In particular, the C-atoms at positions 3 and 9 (marked as deeper red sites in Fig. 3) tend to donate electrons, whereas those at positions 4 and 10, or 5 and 11 (marked as deeper blue sites in Fig. 3) behave like electron-accepting sites during the electronic transition. Chemical intuition suggests that replacing a donor-like C(sp^2) site with an atom with either more electronegative or electron withdrawing character on excitation might disrupt the

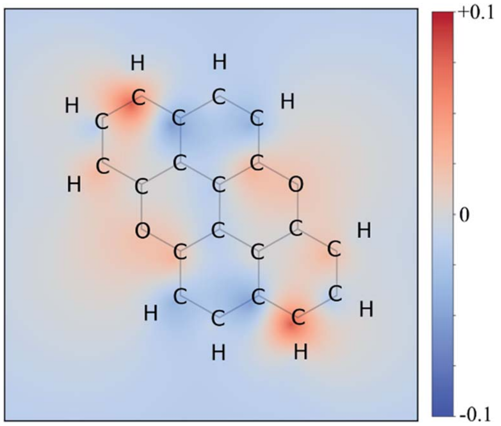

Fig. 3 Excitation charge redistribution map for **PXX**. This is the excited state CHELPG charges minus ground state CHELPG charges of **PXX** interpolated over the atomic positions on the σ-scaffold, with the blue and red area indicating the electron depletion and accumulation regions respectively. The colour map ranges from +0.1 (red, donors) to −0.1 (blue, acceptors) electrons.

PXX excitation pattern, possibly leading to poorer excitation properties (higher excitation energies, lower intensity, for example). For now we assume this to be the case, and this suggests that replacing the C-atoms with N-atoms in positions 3 and 9, *i.e.*, the most electron depleting sites in the charge redistribution map, leads to a hypsochromic shift of the UV-vis absorption envelop when compared to its parent **PXX**.

On the other hand, if the N-replacement happens in electron-enriching positions, a bathochromic shift of the electronic transition is expected as the **PXX** charge redistribution should be enhanced. This is reflected by a shrinking of the optical gap. Consequently, this predicts the largest bathochromic shifts for the 4,11-, 4,10- and 5,11-doping patterns. Between the extreme cases of gap variation, there is also potential for fine-tuning the molecular optical gap. This would be achieved by combining the effects of the two N-dopants in sites that are characterised by a different role (withdrawing/donating/electronegative/electropositive). For the set of regioisomers of interest, the hypothesis that introducing N atoms at electron enriching positions leads to bathochromic shifts and the opposite for electron depleting sites is demonstrated in theory through jointly examining the regioisomer charge redistribution maps and TDDFT excitation energies (Fig. 4).

Similarly, we predict an almost smooth control over the excitation energies depending on the doping configuration. Notably, the TDDFT results suggest that site-specific N-substitution allows a tuning of the optical gap by about 0.46 eV, going from +0.30 eV

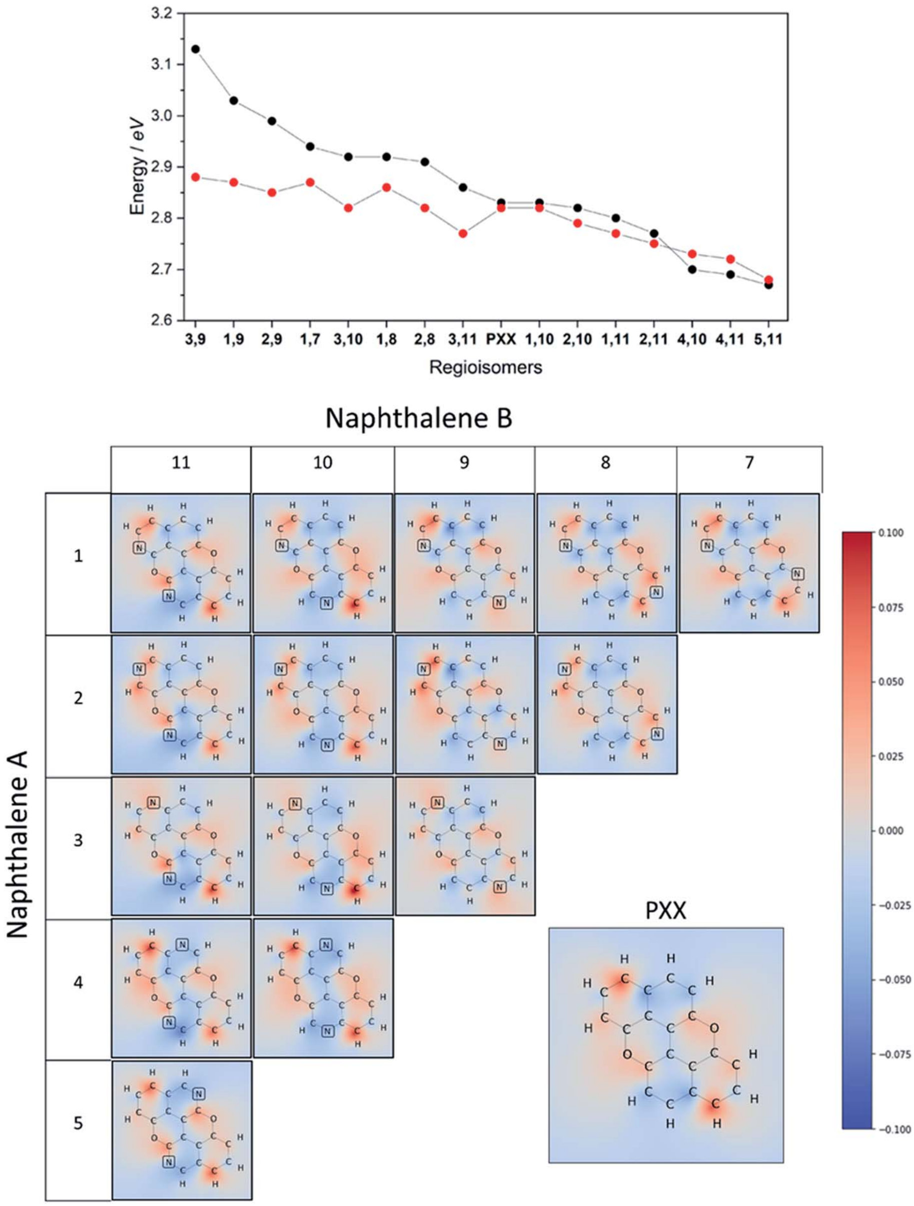

Fig. 4 Top: predicted absorption energy for each positional isomers of *N*,*N*-PXX (DFT in black and Huckel in red). Centre: charge redistribution maps plotted on the σ-scaffold of positional isomers of *N*,*N*-PXX. The colour map ranges from +0.1 (red, donors) to −0.1 (blue, acceptors).

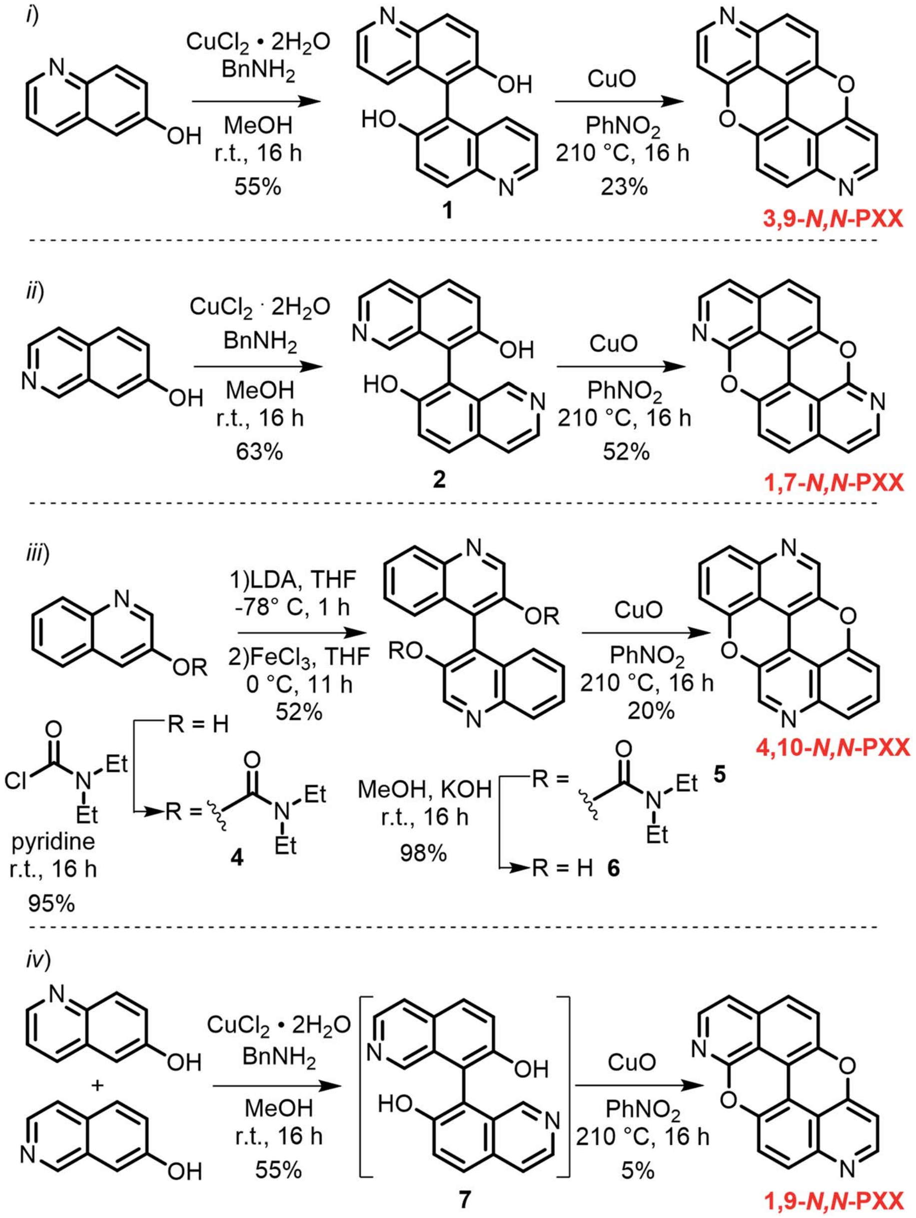

Scheme 1 Synthetic routes to *N*,*N*-PXX: (i) 3,9-*N*,*N*-PXX, (ii) 1,7-*N*,*N*-PXX, (iii) 4,10-*N*,*N*-PXX and (iv) 1,9-*N*,*N*-PXX.

to −0.16 eV with respect to the gap of **PXX**. The final trend is that the 'colour-bleached' excitation maps (when contrasted to **PXX**) lead to hypsochromic shifts, implying that the reduced amount of electron transfer leads to a widening of the optical gap. The influence on transition intensity is more complex and is not discussed extensively here, however, we do highlight trends in the x and y directional components of the transition dipole moment in relation to the doping site. Later in this article, we present spectroscopic measurement of synthesised regioisomers, which validates our electronic structure methodology and approximations through closely matching calculated Franck–Condon lineshapes (see ESI†).

To juxtapose the TDDFT energies, we also present results from calculations using a Hückel tight-binding method (Fig. 4 top).[42,43] This simplified Hamiltonian performs remarkably well in predicting the trend of excitation energies for regioisomers and gives reasonable accuracy when employing an empirical β parameter. The strength of these results is likely explained by examining the character of the TDDFT excitations, as the $S_0 \rightarrow S_1$ transition of these π-conjugated molecules is primarily described (a contribution of more than 96%) by the HOMO → LUMO transfer. We advocate the use of the Hückel calculation to quickly (and exceptionally cheaply) screen the range of excitation energies possible due to doping configurations, however TDDFT results are preferable in this work due to the complete set of accurate *ab initio* properties without the use of the Hückel β.

Finally, it is important to note that the extent of the effect of tuning the optical gap of **PXX** *via* N-substitution is enhanced by the presence of the O-atoms. Indeed, calculations and previous work on the N-doping of anthanthrene show a minor impact on

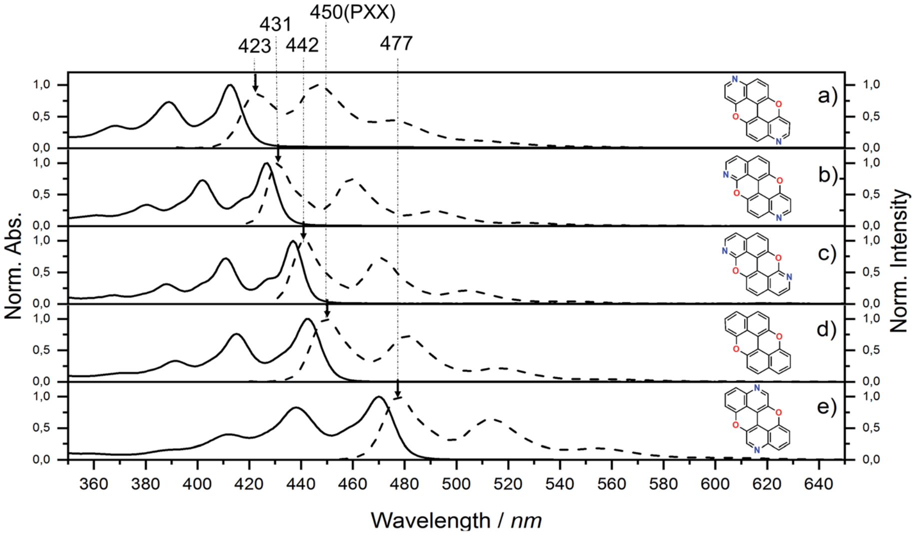

Fig. 5 UV-vis absorption (full line) and emission (dashed line) spectra for *N*,*N*-PXX derivatives and PXX in toluene at rt.

the optical gap, although the trend is the same as that of its **PXX** congener, *i.e.*, the N-substitution of electron depleting and enriching sites causes small blue and bathochromic shifts, respectively (Table S5 and Fig. S17†).

Synthesis

Capitalising on the Cu-mediated Pummerer[44,45] oxidative cyclisation,[31,46] we prepared ***N*,*N*-PXX** derivatives displayed in Scheme 1 following the (i) C–C and (ii) C–O bond formation strategy. Molecule **1** has been prepared following the reported protocol by Kwong.[47] Quinolin-6-ol was dimerised *via* oxidative coupling in the presence of the mixture $CuCl_2$/$BnNH_2$ at room temperature. BIQOL **1** was obtained as a brown solid precipitate in 55% yield and reacted with CuO in $PhNO_2$ under refluxing conditions (210 °C) to give **3,9-*N*,*N*-PXX** in 23% yield. In a parallel avenue, isoquinolin-7-ol was dissolved in MeOH and treated with the $CuCl_2$/$BnNH_2$ complex at rt. BIQOL **2** was collected as brown precipitate and oxidised in the presence of CuO to form **1,7-*N*,*N*-PXX** in 52% yield. When passing to quinolin-3-ol, no C–C coupling product could be formed under the $CuCl_2$/$BnNH_2$ reaction conditions and only starting material was recovered. Increasing the reaction temperature to 120 °C for 16 hours in DMSO led to full conversion, but only a mono O-annulated derivative could be isolated from the reaction mixture (molecule **3** in the ESI†). Thus, we turned our attention to the oxidative dimerization strategy developed by Milicevic and coworkers,[48] who reported the synthesis of BINOLs through oxidative coupling of 1-lithiated naphthol derivatives obtained through *ortho*-metalation. Quinolin-3-ol was dissolved in dry pyridine and treated with carbamoyl chloride to yield carbamate derivative **4** in 95% yield. Treatment of **4** with LDA at −78 °C, followed by the addition of anhydrous $FeCl_3$, gave carbamate-protected BIQOL **5** in 52% yield. Hydrolysis of the carbamoyl moieties with KOH in MeOH yielded BIQOL **6** in 98% that, under CuO-mediated oxidative cyclisation reaction, formed desired molecule **4,10-*N*,*N*-PXX** in 20% yield.

Capitalising on the synthetic routes used to prepare derivatives **1,7-*N*,*N*-PXX** and **3,9-*N*,*N*-PXX**, reference molecule **1,9-*N*,*N*-PXX** was also prepared.[31,47] Isoquinolin-7-ol and quinolin-6-ol were dissolved in MeOH with $CuCl_2$ and $BnNH_2$ and coupled to form a statistical mixture of BIQOL derivatives. Subsequent oxidation with CuO yielded derivative **1,9-*N*,*N*-PXX** as a yellow solid in 5%. Despite the numerous synthetic attempts, we could not prepare any of the ***N*,*N*-PXX** isomers depicting an N atom either at the 2 or 11 position (for further details see the ESI†). All molecules were fully characterised by NMR techniques, HR-MS

Table 1 Photophysical properties of PXX and of its *N*,*N*-PXX derivatives in air-equilibrated toluene at rt

	Absorbance			Emission				Energy gaps	
	λ_{max} (eV) [nm]	ε (M^{-1} cm^{-1})	E^{T}_{exc} (eV)	λ_{max} (eV) [nm]	(ns)	$\Phi_F{}^a$ (%)	Stokes shift (eV) [nm]	$E_g^{opt\,b}$ (eV)	$E_g^{T\,c}$ (eV)
3,9-*N*,*N*-PXX	3.00 [413]	11 838	3.13	2.93 [423]	6.6	75	7×10^{-2} [10]	2.93	3.43
1,9-*N*,*N*-PXX	2.90 [427]	16 667	3.03	2.88 [431]	4.5	64	2×10^{-2} [4]	2.84	3.37
1,7-*N*,*N*-PXX	2.84 [437]	26 611	2.94	2.80 [442]	3.8	61	4×10^{-2} [5]	2.78	3.32
PXX	2.80 [443]	17 560	2.83	2.76 [450]	5	61	4×10^{-2} [7]	2.74	3.30
4,10-*N*,*N*-PXX	2.63 [470]	7448	2.70	2.60 [477]	13.5	41	3×10^{-2} [7]	2.57	3.02

[a] Φ_{fl} measured by optical dilute method and coumarin 153 as reference. [b] $E_g^{opt} = 1240/\lambda_{max}$ (nm). [c] TDDFT calculated value.

Table 2 Half-wave potentials ($E_{ox}^{1/2}$ and $E_{red}^{1/2}$) were determined by CV and referenced *vs.* the Fc^+/Fc couple (solvent: ODCB, 63 mM TBAF)

	$E_{ox}^{1/2a}$ (V) [mV]	$E_{red1}^{1/2}$ ^{a} (V) [mV]	$E_{red2}^{1/2}$ ^{a} (V) [mV]	E_g^{CV} (eV)	E_{red}^* (V)	E_{ox}^* (V)	HOMO^b (eV)	LUMO^b (eV)
3,9-*N*,*N*-PXX	0.71 [148]	−1.81 [116]	n.d.	2.52	−2.22	1.12	−5.81 [−5.68]	−3.29 [−2.52]
1,9-*N*,*N*-PXX	0.71 [115]	−1.83 [125]	n.d.	2.54	−2.13	1.01	−5.81 [−5.67]	−3.27 [−2.28]
1,7-*N*,*N*-PXX	0.63 [167]	−1.87 [97]	n.d.	2.50	−2.15	0.91	−5.73 [−5.66]	−3.23 [−2.30]
PXX	0.30 [119]	−2.59 [148]^c	n.d.	2.89	−2.44	0.15^c	−5.40 [−5.06]	−2.51 [−1.76]
4,10-*N*,*N*-PXX	0.65 [229]	−1.94 [108]	−2.35 [186]	2.59	−1.92	0.63	−5.74 [−5.71]	−3.16 [−2.70]

[a] Half-wave potentials are calculated as $E_{1/2} = (E_{pa} + E_{pc})/2$ considering anodic (E_{pa}) and cathodic (E_{pc}) peak potentials, unless differently specified. Values in parentheses refer to the peak separation ($E_{pa} - E_{pc}$, in mV) of each process; "n.d." stands for "not detected". [c] Values in parentheses are referred to the theoretical values calculated by DFT. [b] Detected in CH_3CN.[3]

spectrometry and single-crystal X-ray diffraction (see section below) analyses.

Photophysical investigations

Steady-state UV-vis absorption and emission measurements were carried out in toluene solutions (Fig. 5 and Table 1). The spectral envelopes of ***N*,*N*-PXX** molecules are similar to that of **PXX**, and are all characterized by $\pi \rightarrow \pi^*$ transitions according to the TDDFT calculations. **PXX** depicts the lowest-energy electronic transition at 443 nm, whereas congeners **3,9-*N*,*N*-PXX**, **1,9-*N*,*N*-PXX**, and **1,7-*N*,*N*-PXX** display blue-shifted bands centred at 413 nm, 427 nm and 437 nm, respectively (Table 1).

Similarly, all emission spectral envelopes of **3,9-*N*,*N*-PXX**, **1,9-*N*,*N*-PXX**, and **1,7-*N*,*N*-PXX** are blue-shifted compared to that of **PXX** (450 nm). In full agreement with our designing principle and theoretical predictions (see the experimental optical and theoretical energy gaps, E_g^{opt} and E_g^T, Table 1), the 3,9-N-doping pattern of molecule **3,9-*N*,*N*-PXX** induces the largest blueshift ($\Delta E_g^{opt} = +0.19$ eV, $E_g^{opt} = 2.74$ eV and 2.93 eV for **PXX** and **3,9-*N*,*N*-PXX**, respectively), as the two most-depleting 3,9-sites in **PXX** have been replaced by two N-atoms. As anticipated by our model, a smaller blueshift of the optical gap was observed ($\Delta E_g^{opt} = +0.1$ eV) with congener **1,7-*N*,*N*-PXX** ($E_g^{opt} = 2.84$ eV), as the 1,7-N-doping pattern is localised to positions in which

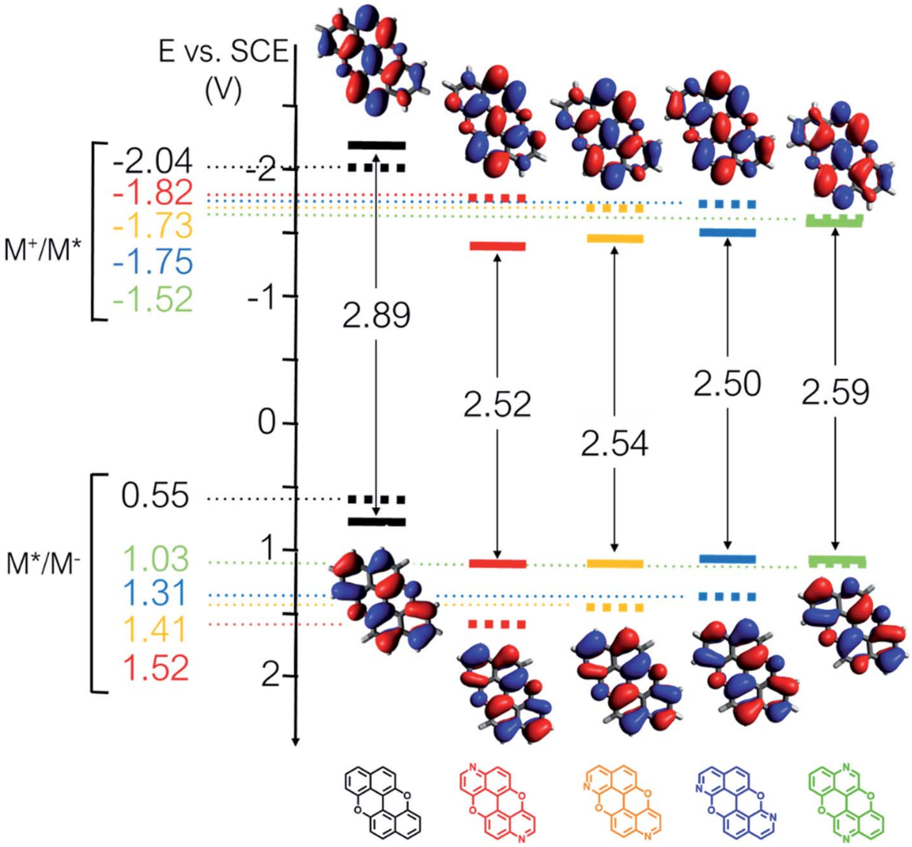

Fig. 6 Redox potentials *vs.* SCE of PXX, 3,9-*N*,*N*-PXX, 1,9-*N*,*N*-PXX, 1,7-*N*,*N*-PXX and 4,10-*N*,*N*-PXX estimated from the CV data obtained in ODCB. Dashed lines: reduction (E_{M^+/M^*}) and oxidation (E_{M^*/M^-}) potentials of the singlet excited states estimated using the optical band gap measured in toluene.[6] Inserts: DFT calculated HOMO (bottom) and LUMO (top) lobes.[6]

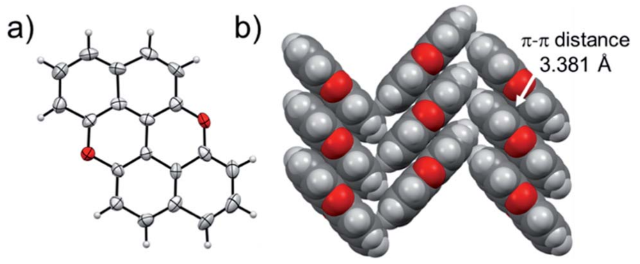

Fig. 7 Single-crystal X-ray structure of **PXX**. ORTEP representation (a) and (b) herringbone-type arrangement. Space groups: $P2_1/c$. Data taken from literature.[52] Atom colours: red O, grey C, white H.

minor electron redistribution occurs. Finally, a bathochromic shift ($\Delta E_g^{opt} = -0.17$ eV) was observed with isomer **4,10-*N*,*N*-PXX**, which depicts the $\pi \rightarrow \pi^*$ transition centred at 470 nm ($E_g^{opt} = 2.57$ eV). As anticipated by our predictive tool, the 4,10-N-doping pattern induces the strongest bathochromic shifts, being the N-atoms overlaying the most electron-enriching sites of **PXX.** While the fluorescence quantum yield (Φ_F) values for **1,9-*N*,*N*-PXX**, **1,7-*N*,*N*-PXX** and **PXX** are virtually the same (~60%, Table 1), a significant enhancement (~75%) was observed for **3,9-*N*,*N*-PXX**, the most blueshifted-absorbing derivative. In contrast, redshifted **4,10-*N*,*N*-PXX** features the lowest Φ_F value (41%). All lifetime values, τ, are within the same range (between 6 and 3 ns), but that for **4,10-*N*,*N*-PXX**, which features the longest value (13.5 ns).

In light of this, the correlation between doping position and the variation of the absorption and emission maxima theoretically postulated was demonstrated since the optical bandgaps of the four positional isomers ***N*,*N*-PXX** follow perfectly the predicted values. Similarly, the TDDFT calculations are validated, showing good accuracy with respect to the optical gap and being only slightly red shifted and under sensitive to the doping pattern. These limitations may be addressed by choice of the exchange correlation functional, however the recreation of the UV-vis lineshapes by Franck–Condon (Fig. S14†) indicates perfectly adequate results here.

Electrochemical investigations

The effect of the N-substitution was also investigated against the redox behaviour of **PXX** (Table 2 and ESI†). Cyclic voltammetry (CV) studies of **PXX** and its ***N*,*N*-PXX** congeners were performed in orthodichlorobenzene (ODCB). As expected all ***N*,*N*-PXX** derivatives displayed higher (of ~0.3–0.4 V) oxidation potentials ($E_{ox}^{1/2} = 0.71$ V, 0.71 V, 0.63 V and 0.65 V for **3,9-*N*,*N*-PXX**, **1,9-*N*,*N*-PXX**, **1,7-*N*,*N*-PXX** and **4,10-*N*,*N*-PXX**, respectively) when compared to that of **PXX** ($E_{ox}^{1/2} = 0.30$ V).

While **PXX** showed no reductive events within the investigated potential window, all ***N*,*N*-PXX** derivatives displayed reversible reduction events. For instance, reversible reduction peaks centred at $E_{red}^{1/2} = -1.81$ V, -1.83 V, and -1.87 V were observed for **3,9-*N*,*N*-PXX**, **1,9-*N*,*N*-PXX** and **1,7-*N*,*N*-PXX**, respectively. Interestingly, the CVs of **4,10-*N*,*N*-PXX** showed two reversible reduction peaks centred at -1.94 V ($E_{red1}^{1/2}$) and -2.35 V ($E_{red2}^{1/2}$), respectively. As expected, these data suggest that the N-doping causes a low-energy rigid shift of the energy levels of the HOMO and LUMO orbitals. When looking at the electrochemical gap (E_g^{CV}), calculated as $E_{ox}^{1/2} - E_{red1}^{1/2}$, the replacement of two C-atoms with N-atoms shrank the E_g^{CV} value of

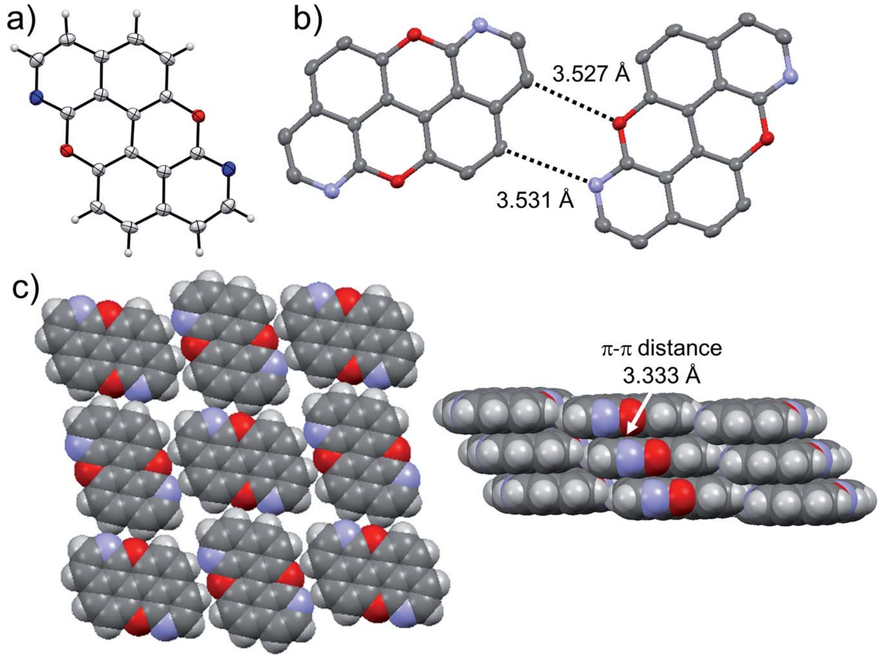

Fig. 8 Single-crystal X-ray structure of **1,7-*N*,*N*-PXX**. ORTEP representation (a) and structure of two isolated molecules engaging into H-bonds (b) depicting a multilayer-type organisation of π–π stacked supramolecular H-bonded sheets (c). Space groups: $P2_1/c$. Atom colours: red O, blue N, grey C, white H.

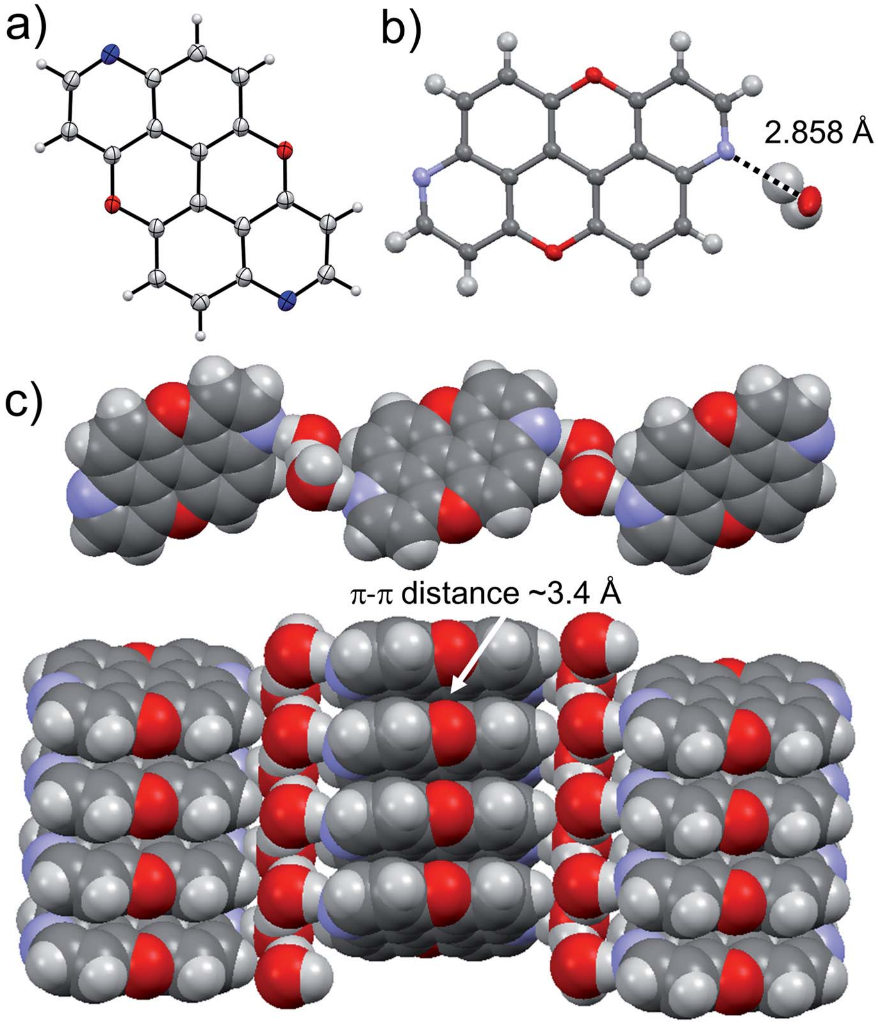

Fig. 9 Single-crystal X-ray structure of **3,9-*N*,*N*-PXX**. ORTEP representation (a) and structure of the water and **3,9-*N*,*N*-PXX** molecules engaging into H-bonds (b) depicting the supramolecular polymer organisation (c). Space groups: $P2_1/c$. Atom colours: red O, blue N, grey C, white H.

around 0.4 V when compared to that of **PXX**. However, the E_g^{CV} values of the ***N*,*N*-PXX** isomers are very similar, with the largest ΔE_g^{CV} (0.09 eV) being that between isomers **1,7-*N*,*N*-PXX** and **4,10-*N*,*N*-PXX** (Table 2). These observations suggest that the doping pattern has a minor impact on the E_g^{CV} value when compared to that of the doping ratio ρ, which is a more influential parameter for the redox properties, *i.e.*, higher oxidations and reduction potentials and a shrank E_g^{CV}, of this class of molecules.

From the combination of photophysical and redox properties, one can estimate the oxidation and reductions of the excited states and thus the photoredox properties of **PXX** and its N-containing congeners (Fig. 6).[6] Consideration of the redox properties in both the excited and ground states is crucial when evaluating and/or tailoring the photochemical reactivity of a chromophore in the context of light-triggered applications (*e.g.*, light-harvesting systems, photosynthesis and photocatalysis to name a few).[6,49–51] From Fig. 6 it is evident that, when comparing the reductive and oxidation properties of the excited states, the ***N*,*N*-PXX** derivatives are respectively stronger oxidisers and weaker reducers at their S_1 states than **PXX**. While the reduction potentials of the S_1 state (E_{M^+/M^*}) within the ***N*,*N*-PXX** series are virtually the same within the experimental errors, the S_1-centered oxidation potential (E_{M^*/M^-}) increases in the order **4,10-*N*,*N*-PXX**, **1,7-*N*,*N*-PXX**, **1,9-*N*,*N*-PXX**, and **3,9-*N*,*N*-PXX** (Fig. 6). The N-pattern has a strong impact on the oxidation property of the S_1 state, with the most hypsochromically- and bathochromically-shifted absorbers being the stronger and weaker oxidisers respectively.

Solid-state self-assembly

At last, we studied the effect of the N-doping on the solid-state organisation of **PXX**. **PXX** undergoes the typical herringbone arrangement of PAHs (Fig. 7),[52] where the molecules organise through edge-to-face and face-to-face ($d_{\pi-\pi} = 3.381$ Å) along the *a* and *c* axes, respectively.[52] The molecule featuring the N-atoms along the 1,7-pattern undertakes a different organisation (Fig. 8). In particular, X-ray diffraction analysis of crystals obtained from slow vapour diffusion of Et_2O into a toluene solution of **1,7-*N*,*N*-PXX** revealed the formation of a non-covalent lamellar

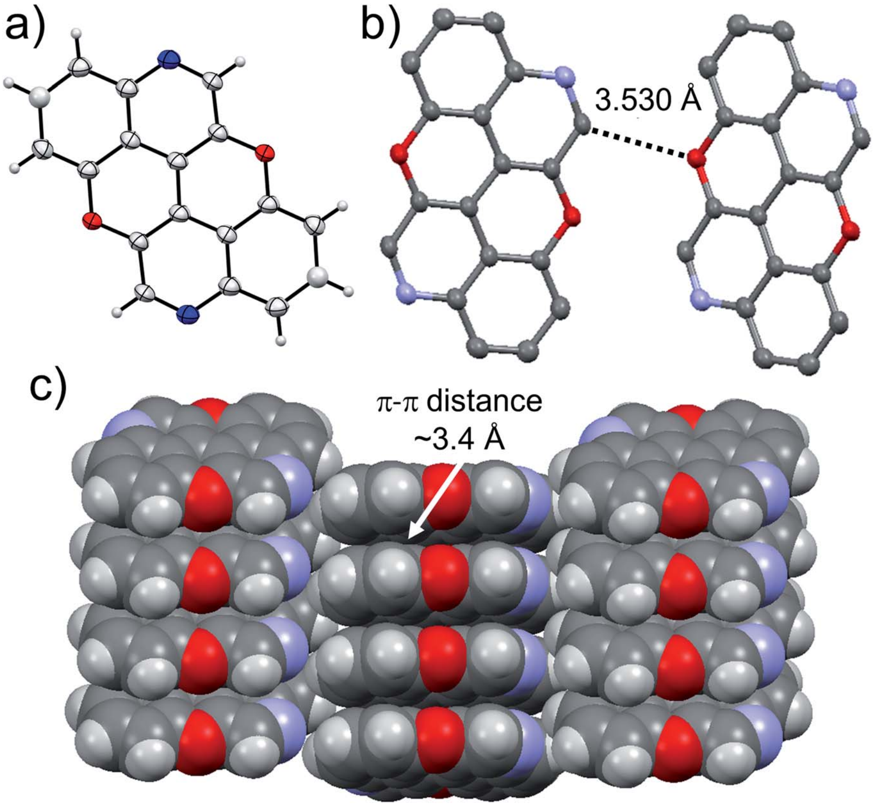

Fig. 10 Single-crystal X-ray structure of **4,10-*N*,*N*-PXX**. ORTEP representation (a) and structure of two molecules engaging into H-bonds (b) forming a columnar organization (c). Space groups: $P2_1/n$. Atom colours: red O, blue N, grey C, white H.

architecture, in which the molecules arrange into supramolecular sheets (*i.e.*, 2D polymeric architecture **(1,7-*N*,*N*-PXX)$_n$**) and are held together by four pairs of weak DD···AA-type H-bonds.

These are established between the side-by-side O and N heteroatoms and the pseudo-*peri* H atoms of a neighbouring molecule. In total, each molecule establishes four H-bonds as donor and four as acceptor. Within the non-covalent sheet, N···C and O···O distances are equal to 3.531 Å and 3.527 Å. At the molecular level, the supramolecular sheets organise in an

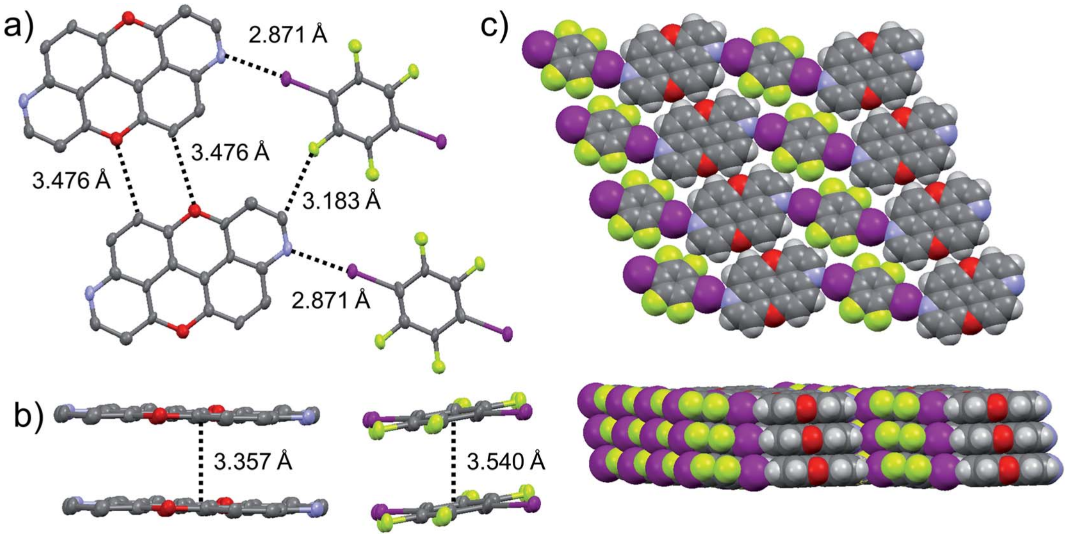

Fig. 11 Single-crystal X-ray structure of co-crystal **3,9-*N*,*N*-PXX·DITFB**. ORTEP representation and structure of four molecules engaging into H-bonds and XBIs (a) organised in supramolecular multi-layered π–π stacked (b) sheets (c). Space groups: $P\bar{1}$. Atom colours: red O, blue N, purple I, green F, grey C, white H.

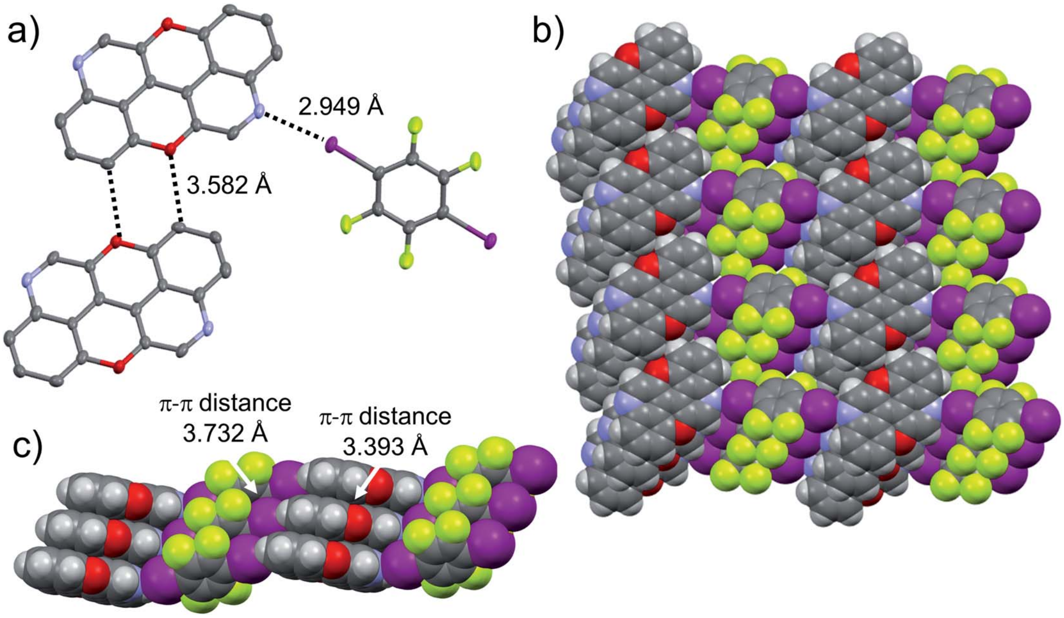

Fig. 12 Single-crystal X-ray structure of co-crystal **4,10-*N*,*N*-PXX·DITFB**. ORTEP representation and structure of three molecules engaging into H-bonds and XBIs (a) organised in supramolecular π–π stacked (b) supramolecular polymers (c). Space groups: $P\bar{1}$. Atom colours: red O, blue N, purple I, green F, grey C, white H.

off-set multilayered, graphite-like, fashion displaying an averaged interplanar π–π stacking distance of 3.333 Å (Fig. 8).

Suitable crystals for X-ray analysis for **3,9-*N*,*N*-PXX** were obtained from slow evaporation of a $CHCl_3$ solution. The analysis revealed the formation of a co-crystal with water in a 1 : 2 ratio with **3,9-*N*,*N*-PXX** (Fig. 9). Interestingly, a supramolecular polymer **(3,9-*N*,*N*-PXX·2H$_2$O)$_n$** is formed through a 1 : 2 association of both components. One can easily discern dimeric associates of the water molecules through an O···H bond ($d_{\mathrm{O\cdots O}} = 2.552$ Å). Each water dimer sandwiches a molecule of **3,9-*N*,*N*-PXX** through two H-bonds established with the quinoline-like N-atoms ($d_{\mathrm{N\cdots O}} = 2.858$ Å). Notably, **3,9-*N*,*N*-PXX** arranges in columnar π–π stacks (estimated $d_{\pi-\pi} = 3.4$ Å) separated by a layer of dimeric water molecules (Fig. 9). The solid-state arrangement led to a segregation between the hydrophilic and non-hydrophilic moieties.

At last, we studied the solid-state organisation of isomer **4,10-*N*,*N*-PXX**. The crystals were grown by slow diffusion of hexane vapours into a $CHCl_3$ solution of **4,10-*N*,*N*-PXX.** Only a columnar arrangement was observed (Fig. 10), with the molecule undergoing off-set face-to-face π–π stacking (estimated $d_{\pi-\pi} = 3.4$ Å). The columnar stacks (Fig. 10) lies each other through very weak C–H···O bonds ($d_{\mathrm{C-H\cdots O}} = 3.530$ Å).

The presence of the nucleophilic quinoline-like N-atoms offered us the possibility to exploit halogen-bonding interactions (XBIs) to govern the solid-state organisation. Thus, we independently co-crystallized molecules **3,9-*N*,*N*-PXX** and **4,10-*N*,*N*-PXX** with 1,4-diiodo-2,3,5,6-tetrafluorobenzene (**DITFB**) in a 1 : 1 ratio, and grew crystals from slow evaporation of a $CHCl_3$ solution. As expected, in both cases the given ***N*,*N*-PXX** derivatives undergo XBIs with **DITFB**, giving rise to halogen-bonded complexes **3,9-*N*,*N*-PXX·DITFB** and **4,10-*N*,*N*-PXX·DITFB**, respectively. In the case of **3,9-*N*,*N*-PXX·DITFB**, a supramolecular polymeric ribbon **(3,9-*N*,*N*-PXX·DITFB)$_n$** was formed at the solid state (Fig. 11). The structure displays the quinoline-like moieties establishing XBIs ($d_{\mathrm{N\cdots I}} = 2.871$ Å) with **DITFB**, with its tetrafluoroaryl core being coplanar with the polycyclic ring of **3,9-*N*,*N*-PXX.** The halogen-bonded ribbons arrange through lateral weak H-bonds ($d_{\mathrm{O\cdots C}} = 3.476$ Å) in striped patterned sheets. The sheets arrange in multilayers through π–π stacking interactions, where the fluorinated and non-fluorinated moieties are segregated and the **3,9-*N*,*N*-PXX** and **DITFB** modules engage with homomolecular off-set π–π stacking interactions ($d_{\pi-\pi} = 3.357$ Å and 3.540 Å, off-set of 0.85 Å and 1.43 Å, Fig. 11). Also **4,10-*N*,*N*-PXX·DITFB** organises in supramolecular polymeric ribbons **(4,10-*N*,*N*-PXX·DITFB)$_n$** at the solid state (Fig. 12). In this case, longer-distance XBIs ($d_{\mathrm{N\cdots I}} = 2.949$ Å) are established between the halogen acceptor and donor molecules, which are also segregated in fluorinated and non-fluorinated domains. In contrast to **(3,9-*N*,*N*-PXX·DITFB)$_n$**, the monomeric units in polymer **(4,10-*N*,*N*-PXX·DITFB)$_n$** are not coplanar (*i.e.*, the aromatic cores of **4,10-*N*,*N*-PXX** and **DITFB** are not coplanar) and terraced layers are formed (Fig. 12). Neighbouring supramolecular polymers are held together by lateral very weak H-bonds ($d_{\mathrm{O\cdots C}} = 3.582$ Å). Similarly to the case of co-crystal **3,9-*N*,*N*-PXX·DITFB**, molecules **4,10-*N*,*N*-PXX** and **DITFB** engage with homomolecular π–π stacking interactions ($d_{\pi-\pi} = 3.393$ Å and 3.732 Å, off-set of 1.04 Å and 1.42 Å, Fig. 12).

Conclusion

In this paper we have raised the question of whether (i) we can rationally tailor the optical bandgap properties of a PAH by a specific heteroatom doping pattern and (ii) if this can be predicted *a priori* to guide organic chemists in the structural design. Thus, we have developed a predictive tool that identifies C(sp^2)-positions in the π-conjugated core of a given PAH that, if substituted with a heteroatom, would cause the desired changes in the UV-vis absorption and emission spectral envelopes. Using *peri*-xanthenoxanthene (**PXX**) as a model polyaromatic hydrocarbon, we showed that TDDFT calculations of the electron density difference between the S_1 excited state and S_0 ground state of **PXX** allowed us to identify the subtleties in the role of atomic sites, *i.e.*, electron withdrawing or donating abilities, on the excitation energy. Specifically, we have found that the replacement of two C(sp^2)-atoms with two N-atoms in either electron donating or withdrawing positions, shift the electronic transitions either bathochromically or hypsochromically, respectively. To validate the predictive tool, we synthesised a series of N-doped **PXX** positional isomers peripherally bearing one N-atom for each naphthalenyl ring and characterized their electronic transitions by means of steady-state absorption and emission UV-vis spectroscopies. In full agreement with theoretical predictions, the spectral envelops of the N-doped **PXX** derivatives depicting the N atoms in the most-depleting sites are blueshifted when compared to that of **PXX** (with **3,9-*N*,*N*-PXX** displaying the largest shift: +0.19 eV). On the other hand, when overlaying the N-pattern on the most electron-enriching sites of **PXX**, a bathochromic shift of the absorption bands was observed (−0.17 eV for **4,10-*N*,*N*-PXX**), as anticipated by our predictive tool. Fluorescence quantum yield measurements show the more blueshifted the absorption/emission energies, the greater the Φ_F value (from ~41% to ~75%). Surprisingly, CV studies suggested that the redox properties are only marginally affected by the N-pattern and all ***N*,*N*-PXX** depict very similar redox properties at the ground state. Lastly, we have studied the solid-state organisation of the N-doped **PXX**, and showed that the N-pattern has a strong impact on the supramolecular architecture. While the ***N*,*N*-PXX** derivative depicting the 1,7-pattern forms multi-layered, graphene-like supramolecular sheets, the 3,9- and 4,10-congeners self-assemble into wire-like polymeric architectures. When the **3,9-** and **4,10-*N*,*N*-PXX** derivatives are co-crystallized with a halogen-bond donor molecule, supramolecular striped patterned sheets are formed.

To the best of our knowledge, this work describes the first design of heteroatom-doped PAHs in which charge-redistribution maps of singlet-state excitations are used to rationally conceive the doping patterns tailoring a given electronic energy transition. This simple approach can be generalised and assists organic chemists to conceive tailored chromophores *via* specific doping patterns, thus minimising synthetic efforts.

Conflicts of interest

There are no conflicts to declare.

Data availability

All the data supporting this article have been included in the main text and the ESI.†

Author contributions

CV carried out all organic synthetic work, structural characterisation, electrochemical studies and UV-vis steady-state, spectroscopic absorption and emission studies and interpreted the data with DB. DG performed all the DFT calculations, computed the charge-redistribution maps and interpreted the data with NB. GB prepared and characterised molecule **1,9-*N*,*N*-PXX**. DR performed the X-ray diffraction analysis and solved the X-ray structure for all molecules but derivative **3**, which was performed by ND. DB conceived and coordinated the project and conceptualised the content of the manuscript together with NB and DG. All authors participated in discussing the data and wrote the manuscript.

Acknowledgements

D. B. gratefully acknowledge the EU through the MC-RISE "INFUSION" and H2020-IA "DecoChrom" projects, the School of Chemistry at Cardiff University (CA) and the University of Vienna for financial support. CV thanks the School of Chemistry at CA for his doctoral fellowship. D. G. and N. B. acknowledge the supportive research environment of the EPSRC Centre for Doctoral Training in Cross-Disciplinary Approaches to Non-Equilibrium Systems (CANES, No. EP/L015854/1) and the U.K. Materials and Molecular Modelling Hub (MMM Hub) for compute resources, which is partially funded by EPSRC (EP/P020194/1).

References

1 O. Kulyk, L. Rocard, L. Maggini and D. Bonifazi, *Chem. Soc. Rev.*, 2020, **49**, 8400–8424.
2 C. Pezzetta, A. Folli, O. Matuszewska, D. Murphy, R. W. M. Davidson and D. Bonifazi, *Adv. Synth. Catal.*, 2021, **363**, 4740–4753.
3 A. Sciutto, A. Fermi, A. Folli, T. Battisti, J. M. Beames, D. M. Murphy and D. Bonifazi, *Chem.–Eur. J.*, 2018, **24**, 4382–4389.
4 A. L. Trifonov, L. I. Panferova, V. V. Levin, V. A. Kokorekin and A. D. Dilman, *Org. Lett.*, 2020, **22**, 2409–2413.
5 Q. Ma, J. Song, X. Zhang, J. Yu, L. Ji and S. Liao, *Nat. Commun.*, 2021, **12**, 429.
6 A. Fermi and D. Bonifazi, *Photochemistry*, 2020, **47**, 293–325.
7 A. Borissov, Y. K. Maurya, L. Moshniaha, W.-S. Wong, M. Zyła-Karwowska and M. Stępien, *Chem. Rev.*, 2021, **122**, 565–788.
8 M. Stępień, E. Gońka, M. Żyła and N. Sprutta, *Chem. Rev.*, 2017, **117**, 3479–3716.
9 A. Narita, X. Y. Wang, X. Feng and K. Müllen, *Chem. Soc. Rev.*, 2015, **44**, 6616–6643.
10 D. B. Granger, Y. Mei, K. J. Thorley, S. R. Parkin, O. D. Jurchescu and J. E. Anthony, *Org. Lett.*, 2016, **18**, 6050–6053.
11 Y. S. Park, D. J. Dibble, J. Kim, R. C. Lopez, E. Vargas and A. A. Gorodetsky, *Angew. Chem., Int. Ed.*, 2016, **55**, 3352–3355.

12 A. Riaño, K. Strutyński, M. Liu, C. T. Stoppiello, B. Lerma-Berlanga, A. Saeki, C. Martí-Gastaldo, A. N. Khlobystov, G. Valenti, F. Paolucci, M. Mell and A. Mateo-Alonso, *Angew. Chem., Int. Ed.*, 2021, **61**, e202113657.

13 R. K. Dubey, M. Melle-Franco and A. Mateo-Alonso, *J. Am. Chem. Soc.*, 2021, **143**, 6593–6600.

14 D. Lehnherr, J. M. Alzola, C. R. Mulzer, S. J. Hein and W. R. Dichtel, *J. Org. Chem.*, 2017, **82**, 2004–2010.

15 L. Ji, A. Friedrich, I. Krummenacher, A. Eichhorn, H. Braunschweig, M. Moos, S. Hahn, F. L. Geyer, O. Tverskoy, J. Han, C. Lambert, A. Dreuw, T. B. Marder and U. H. F. Bunz, *J. Am. Chem. Soc.*, 2017, **139**, 15968–15976.

16 Z. Zeng, H. Jin, K. Sekine, M. Rudolph, F. Rominger, A. Stephen and K. Hashmi, *Angew. Chem., Int. Ed.*, 2018, **57**, 6935–6939.

17 P. Karak, C. Dutta, T. Dutta, A. L. Koner and J. Choudhury, *Chem. Commun.*, 2019, **55**, 6791–6794.

18 U. H. F. Bunz and J. Freudenberg, *Acc. Chem. Res.*, 2019, **52**, 1575–1587.

19 C. L. Deng, J. P. Bard, L. N. Zakharov, D. W. Johnson and M. M. Harley, *Org. Lett.*, 2019, **21**, 6427–6431.

20 B. L. Hu, C. An, M. Wagner, G. Ivanova, A. Ivanova and M. Baumgarten, *J. Am. Chem. Soc.*, 2019, **141**, 5130–5134.

21 J. P. Mora-Fuentes, A. Riaño, D. Cortizo-Lacalle, A. Saeki, M. Melle-Franco and A. Mateo-Alonso, *Angew. Chem., Int. Ed.*, 2018, **58**, 552–556.

22 K. Jug and G. Hahn, *J. Comput. Chem.*, 1983, **4**, 410–418.

23 R. M. Hochstrasser and J. W. Michaluk, *J. Chem. Phys.*, 1971, **55**, 4668.

24 D. Stassen, N. Demitri and D. Bonifazi, *Angew. Chem., Int. Ed.*, 2016, **55**, 5947–5951.

25 A. Berezin, N. Biot, T. Battisti and D. Bonifazi, *Angew. Chem., Int. Ed.*, 2018, **57**, 8942–8946.

26 A. Sciutto, A. Berezin, M. Lo Cicero, T. Miletić, A. Stopin and D. Bonifazi, *J. Org. Chem.*, 2018, **83**, 13787–13798.

27 L. Đorđević, C. Valentini, N. Demitri, C. Mézière, M. Allain, M. Sallé, A. Folli, D. Murphy, S. Mañas-Valero, E. Coronado and D. Bonifazi, *Angew. Chem., Int. Ed.*, 2019, **59**, 4106–4114.

28 J. A. Christensen, J. Zhang, J. Zhou, J. N. Nelson and M. R. Wasielewski, *J. Phys. Chem. C*, 2018, **122**, 23364–23370.

29 C. Song and T. M. Swager, *Macromolecules*, 2009, **42**, 1472–1475.

30 N. Lv, M. Xie, W. Gu, H. Ruan and S. Qiu, *Org. Lett.*, 2013, **15**, 2382–2385.

31 T. Miletić, A. Fermi, I. Orfanos, A. Avramopoulos, F. De Leo, N. Demitri, G. Bergamini, P. Ceroni, M. G. Papadopoulos, S. Couris and D. Bonifazi, *Chem.–Eur. J.*, 2017, **23**, 2363–2378.

32 N. Kobayashi, M. Sasaki and K. Nomoto, *Chem. Mater.*, 2009, **21**, 552–556.

33 M. Noda, N. Kobayashi, M. Katsuhara, A. Yumoto, S. Ushikura, R. Yasuda, N. Hirai, G. Yukawa, I. Yagi, K. Nomoto and T. Urabe, *SID Symp. Dig. Tech. Pap.*, 2010, **41**, 710–713.

34 A. D. Becke, *J. Chem. Phys.*, 1993, **98**, 5648–5652.

35 C. Lee, W. Yang and R. G. Parr, *Phys. Rev. B: Condens. Matter Mater. Phys.*, 1988, **37**, 785–789.

36 S. H. Vosko, L. Wilk and M. Nusair, *Can. J. Phys.*, 1980, **58**, 1200–1211.

37 P. J. Stephens, F. J. Devlin, C. F. Chabalowski and M. J. Frisch, *J. Phys. Chem.*, 2002, **98**, 11623–11627.

38 T. Clark, J. Chandrasekhar, G. W. Spitznagel and P. V. R. Schleyer, *J. Comput. Chem.*, 1983, **4**, 294–301.

39 R. Krishnan, J. S. Binkley, R. Seeger and J. A. Pople, *J. Chem. Phys.*, 1980, **72**, 650.

40 M. J. Frisch, G. W. Trucks, H. B. Schlegel, G. E. Scuseria, M. A. Robb, J. R. Cheeseman, G. Scalmani, V. Barone, G. A. Petersson, H. Nakatsuji, X. Li, M. Caricato, A. Marenich, J. Bloino, B. G. Janesko, R. Gomperts, B. Mennucci, H. P. Hratchian, J. V. Ortiz, A. F. Izmaylov, J. L. Sonnenberg, D. Williams-Young, F. Ding, F. Lipparini, F. Egidi, J. Goings, B. Peng, A. Petrone, T. Henderson, D. Ranasinghe, V. G. Zakrzewski, J. Gao, N. Rega, G. Zheng, W. Liang, M. Hada, M. Ehara, K. Toyota, R. Fukuda, J. Hasegawa, M. Ishida, T. Nakajima, Y. Honda, O. Kitao, H. Nakai, T. Vreven, K. Throssell, J. A. J. Montgomery, J. E. Peralta, F. Ogliaro, M. Bearpark, J. J. Heyd, E. Brothers, K. N. Kudin, V. N. Staroverov, T. Keith, R. Kobayashi, K. J. Normand, K. Raghavachari, A. Rendell, J. C. Burant, S. S. Iyengar, J. Tomasi, M. Cossi, J. M. Millam, M. Klene, C. Adamo, R. Cammi, J. W. Ochterski, R. L. Martin, K. Morokuma, O. Farkas, J. B. Foresman and D. J. Fox, *Gaussian 09, Revision A.02*, 2016.

41 C. M. Breneman and K. B. Wiberg, *J. Comput. Chem.*, 1990, **11**, 361–373.

42 Y. Carissan, D. Hagebaum-Reignier, N. Goudard and S. Humbel, *J. Phys. Chem. A*, 2008, **112**, 13256–13262.

43 Y. Carissan, D. Hagebaum-Reignier, D. N. Goudard and S. Humbel, 2008, **http://www.hulis.free.fr**.

44 R. Pummerer and A. Rieche, *Ber. Dtsch. Chem. Ges.*, 1926, **59**, 2161–2175.

45 R. Pummerer and F. Frankfurter, *Ber. Dtsch. Chem. Ges.*, 1914, **47**, 1472–1493.

46 T. Kamei, M. Uryu and T. Shimada, *Org. Lett.*, 2017, **19**, 2714–2717.

47 Y. X. Chen, L. W. Yang, Y. M. Li, Z. Y. Zhou, K. H. Lam, a. S. Chan and H. L. Kwong, *Chirality*, 2000, **12**, 510–513.

48 P. R. Blakemore, C. Kilner and S. D. Milicevic, *J. Org. Chem.*, 2005, **70**, 373–376.

49 N. A. Romero and D. A. Nicewicz, *Chem. Rev.*, 2016, **116**, 10075–10166.

50 M. H. Shaw, J. Twilton and D. W. C. MacMillan, *J. Org. Chem.*, 2016, **81**, 6898–6926.

51 L. Buzzetti, G. E. M. Crisenza and P. Melchiorre, *Angew. Chem., Int. Ed.*, 2019, **58**, 3730–3747.

52 T. Asari, N. Kobayashi, T. Naito and T. Inabe, *Bull. Chem. Soc. Jpn.*, 2001, **74**, 53–58.